JGR Space Physics

RESEARCH ARTICLE
10.1029/2019JA026759

Special Section:
Long-term changes and Trends in the Middle and Upper Atmosphere

Solar Response and Long-Term Trend of Midlatitude Mesopause Region Temperature Based on 28 Years (1990–2017) of Na Lidar Observations

Chiao-Yao She[1], U. Berger[2], Zhao-Ai Yan[3,4], Tao Yuan[5,6], F.-J. Lübken[2], David A. Krueger[1], and Xiong Hu[3]

[1]Physics Department, Colorado State University, Fort Collins, CO, USA, [2]Leibniz Institute of Atmospheric Physics, Kühlungsborn, Germany, [3]National Space Science Center, Chinese Academy of Sciences, Beijing, China, [4]College of Materials Science and Opto-Electronic Technology, University of Chinese Academy of Sciences, Beijing, China, [5]Center for Atmospheric and Space Sciences, Utah State University, Logan, UT, USA, [6]Physics Department, Utah State University, Logan, UT, USA

Abstract We present midlatitude solar response and linear trend from Colorado State University/Utah State University Na lidar nocturnal temperature observations between 1990 and 2017. Along with the nightly mean temperatures (_Ngt), we also use the corresponding 2-hr means centered at midnight (_2MN), resulting in vertical trend profiles similar in shapes as those previously published. The 28-year trend from _Ngt (_2MN) data set starts from a small warming at 85 km, to cooling at 87 (88) km, reaching a maximum of 1.85 ± 0.53 (1.09 ± 0.74) at 92 (93) km and turns positive again at 102 (100) km. The 6-month winter trend is much cooler than the 4-month summer trend with comparable solar response varying around 5 ± 1 K/100 SFU throughout the profile (85–105 km) with higher summer values. We explore the observed summer/winter trend difference in terms of observed gravity wave heat flux heating rate at a nearby station and the long-term trend of gravity wave variance at a midlatitude. Between 89 and 100 km, the lidar trends are within the error bars of the Leibniz Middle Atmosphere (LIMA) summer trends (1979–2013), which are nearly identical to the lidar-Ngt trend. We address the need of long data set for reliable analysis on trend, the extent of trend uncertainty due to possible tidal bias, the effect of a Pinatubo/episodic function, and the impact of stratospheric ozone recovery.

Plain Language Summary Anthropogenic greenhouse gases, primarily CO_2, alter the Earth's climate, causing warming in the troposphere and the Earth/ocean surface, and cooling in the middle and upper atmosphere. Although determination of the long-term temperature trend in the important mesopause region, about 100 km from Earth surface where the annual mean temperature is lowest, from ground is very challenging, it has been measured using fluorescence lidar observations. Based on 28-year (1990–2017) data sets of nightly means and 2-hr means centered at midnight, the maximum cooling rates in a midlatitude mesopause region are 1.85 K/decade and 1.09 K/decade, respectively, with the latter thought to be relatively free from contamination by atmospheric tides. The winter trend is much cooler than the summer trend. We found good agreement in the summer trend with model prediction and the summer/winter difference correlate with the associated gravity wave heat flux convergence.

Key Points:
- We deduced long-term solar response and linear trend from 28 years lidar observed midlatitude mesopause region nocturnal temperatures
- We compared the linear trends between nightly mean and 2-hr midnight mean temperatures, and those between all, 4-month summer and 6-month winter
- We found good agreement and trend model prediction and correlation between the summer/winter difference and the associated gravity wave heat flux convergence

Correspondence to:
C.-Y. She,
joeshe@colostate.edu

Citation:
She, C.-Y., Berger, U., Yan, Z.-A., Yuan, T., Lübken, F.-J., Krueger, D. A., & Hu, X. (2019). Solar response and long-term trend of midlatitude mesopause region temperature based on 28 years (1990–2017) of Na lidar observations. *Journal of Geophysical Research: Space Physics*, *124*. https://doi.org/10.1029/2019JA026759

Received 27 MAR 2019
Accepted 7 JUL 2019
Accepted article online 15 JUL 2019

1. Introduction

It is well established that anthropogenic greenhouse gases, primarily CO_2, alter the Earth's climate, causing warming in the troposphere and the Earth/ocean surface, and cooling in the middle and upper atmosphere. Since Roble and Dickinson (1989) modeled the dramatic cooling in the stratosphere, mesosphere, and thermosphere due to doubling of CO_2 and CH_4, progress in both observation and modeling of the greenhouse gas impact on the long-term climatic change has been steady; these have been reviewed by Beig (2011), Cnossen (2012), Qian et al. (2013), and Laštovička (2013, 2017). Second to CO_2, ozone plays an important role (Akmaev et al., 2006) as is evidenced, for example, by the observed change in the low-frequency ionospheric reflection height during the period of dramatic ozone depletion in 1979–1995 (Bremer & Peters, 2008).

The cumulative effect of cooling upward from stratosphere causes shrinking in the middle and upper atmosphere, leading to differences between vertical profiles in pressure altitudes and geometric altitudes

(Akmaev & Fomichev, 1998; Lübken et al., 2013). As the mean temperature gradient changes from negative in the upper mesosphere to positive in lower thermosphere, cooling as a function of pressure altitude may become warming as a function of geometric altitude. This difference is particularly important as one compares the model prediction (carried out in the pressure coordinate for simplicity in analysis) to observation (by necessity in the geometric coordinate). Though accessible by metal (Na, K, and Fe) fluorescence lidars, observations in the mesosphere and lower thermosphere (MLT) are rare, making a direct comparison between models and observations particularly challenging, and thus far preventing the joining of the trends between upper atmosphere and stratosphere into one picture (Laštovička, 2017).

Due perhaps to data sets shorter than necessary, most of the cooling trends deduced from early observations at a local site in the MLT were found to be much larger than ~1 K/decade predicted by a chemical model constrained by the observed lowering rate of Na density centroid height (Clemesha et al., 2004) and ~0.5 K/decade in global cooling temperature trend between 85 and 100 km by the Whole Atmosphere Community Climate Model, version 3 (WACCM3) for the period 1970–2003 (Garcia et al., 2007). She et al. (2009) tabulated these observed long-term temperature trends ranging from 0 to ~10 K/decade and suggested, as did in Beig (2006), that after two decades the observed trend remains inconclusive. They also reported the first comparison of temperature trend profiles (85 to 105 km) between Na lidar observed nocturnal temperatures (1990–2007) at Fort Collins, Colorado (41°N, 105°W) and two models, the Spectral Mesosphere/Lower Thermosphere Model (SMLTM, 1980–2000) and the Hamburg Model of the Neutral and Ionized Atmosphere (HAMMONIA, 1970–1990). Though the 20-year model runs covered different time periods, the observed lidar trend, with max cooling of ~1.5 ± 1.15 K/decade at 91 km and turning to warming trend above 103 km, is consistent with both model predictions in both magnitude and shape of the vertical profile. A later publication (She et al., 2015) based on a combined data set, 1990–2010 at Colorado State University and 2010–2017 at Utah State University (42°N, 112°W) with higher spatial resolution (2.0-km vertical resolution instead of 3.7-km resolution) between 1990 and 2014, yielded similar results (within error bars) with "a cooling trend starting from a statistically insignificant value of 0.64 ± 0.99 K/decade at 85 km, increasing to a maximum of 2.8 ± 0.58 K/decade between 91 and 93 km, and then becoming a warming trend above 103 km." Though the shape of the trend profile from the 25-year data set is similar, the maximum trend, though still within the error bars of the two analyses, is cooler by more than 1.0 K/decade.

Recent observations of mesopause region trends based on OH* temperature (at ~87 km) at different locations resulted in inconsistent pattern of temperature trends (Kalicinsky et al., 2016; Offermann et al., 2010). With global coverage (48°S to 48°N), the trend based on Sounding of the Atmosphere using Broadband Emission Radiometry (SABER) on board the Thermosphere Ionosphere Mesosphere and Dynamics temperatures (2002–2012) was published (Huang et al., 2014). The rarely reported response to the 11-year solar cycle based on the same SABER measurements (2002–2015) was also published (Gan et al., 2017). These SABER results are compared to the most recent lidar results later in this paper. Utilizing meteor wind radar between October 2001 and October 2012 at Svalbard (78°N, 16°E) calibrated by satellite measurements, Hall et al. (2012) reported a temperature trend at 90 km of -4 ± 2 K/decade. A later report (Holmen et al., 2016) based on the same technique at a similar latitude (Tromso, 70N) between 2003 and 2014, however, reported trend of -2.2 ± 1.0 K/decade. Like the SABER trend, the data length of these meteor radar trends may be too short for a robust linear trend determination (Laštovička, 2017). The effect of ozone concentration change on temperature trend and the atmospheric shrinking effect has been comprehensively studied using the LIMA model driven by the European Centre for Medium-Range Weather Forecasts reanalysis below ~40 km (Berger & Lübken, 2011; Lübken et al., 2013). Unlike the modeling of long-term trend, which typically turns off the effect of solar flux variability by considering perpetual solar minimum condition (Solomon et al., 2018), the observed data by necessity include the effect of solar flux variation in the time series. As the result, the fit function must include terms corresponding to solar response and long-term change (trend). Since these two terms in the fit function are not orthogonal to each other, to ensure the accuracy of both responses, a data set should be longer than two solar cycles (Laštovička, 2013).

The main purpose of this paper is to report both solar response and linear trend of nocturnal temperatures at a midlatitude region based on 28 years (1990–2017) of Na lidar observation. We analyze long-term solar responses and linear trends of mesopause-region temperatures based on 4-month summer (May–August) and 6-month winter (October–March), along with all year data. First, our data set and regression analysis strategy is detailed to facilitate the examination of possible uncertainties caused by insufficient data

length, the difference in Pinatubo/episodic (from here on called Pinatubo for simplicity) responses, and possible tidal and short-period contaminations. In section 2 we present our data sets and justify the fit function to be used in this study. Our main lidar results in section 3 are based on both the nightly mean (_Ngt) temperatures and on the 2-hr midnight mean (_2MN) temperatures. Here, we report and compare results using all/annual, 4-month summer and 6-month winter data. These results are then compared to the most recent SABER observations and the newly extended LIMA predictions for summer months (1979–2013) in section 4. In section 5, we discuss the effects of data length, of Pinatubo response, of gravity wave heat flux divergence, and of stratospheric ozone partial recovery (since 1995/1996) on temperature trend and solar response. A brief conclusion follows in section 6.

2. The 28-Year Temperature Series and Regression Analysis

The Colorado State University Na lidar performed nocturnal mesopause region temperature observations between March 1990 and March 2010 at Fort Collins, CO (41°N, 105°W). A vertical beam between 1990 and 2001 measured Na density and mesopause region temperature using two frequencies. Since 2002, the lidar has operated in 2- or 3-beam geometry for simultaneous temperature and horizontal wind measurements using three frequencies, leading to two or three temperatures at a given altitude each night. The inverse-error-square weighted average of two or three very similar values are taken to be the observed temperature. The lidar was relocated to Utah State University campus and has continued its regular observation at Logan, Utah (42°N, 112°W) since September 2010. Because of similar geographical coordinates, we combine the data from both locations to form data sets of nightly mean (_Ngt) and 2-hr midnight mean (_2MN) temperatures from March 1990 to December 2017. The continuity of this data set has been further demonstrated in recent investigation (Yuan et al., 2019).

2.1. Justification of the Fit Function

The nightly temperature in the MLT is known to vary with seasons (with annual and semiannual variations) in addition to a long-term linear trend and a response to solar flux variability. The fit function to a long time series is well known and was given in our previous publications (She et al., 2009, 2015) as:

$$\begin{aligned} T(z,t) &= T_{fit}(z,t) + T_{\mathrm{Res}}(z,t), \ \text{ where} \\ T_{fit}(z,t) &= \alpha(z) + A_1(z)\cos(2\pi t) + B_1(z)\sin(2\pi t) + A_2(z)\cos(4\pi t) + B_2(z)\sin(4\pi t) \\ &\quad +\beta(z)t + \gamma(z)P(z,t) + \delta(z)Q_{81}(t), \ \text{ with } \ P(z,t) = 2/\{\exp(t_0(z)-t)/t_1(z) + \exp(t-t_0(z)/t_2(z)\} \end{aligned} \tag{1}$$

where t is time (each night with data) in the unit of years from 1 January 1990, with $T_{\mathrm{fit}}(z, t)$ and $T_{\mathrm{Res}}(z, t)$ as the best fit and residual, respectively. There are 11 fit parameters in $T_{\mathrm{fit}}(z, t)$ with a number of prescribed proxy base functions of time: α (z) the time-independent term, and the four A–B terms representing annual and semiannual variations, along with three terms with amplitudes $\beta(z)$, $\gamma(z)$, and $\delta(z)$. The linear trend is $\beta(z)$ in K/year. Due to the existence of a strong warming episode in our data, attributable to the Mount Pinatubo eruption in June 1991 (She et al., 1998), a term with amplitude $\gamma(z)$ times an impulse proxy base function $P(z,t)$ is included, with parameters $t_0(z)$, $t_1(z)$, and $t_2(z)$, respectively for the delay, rise, and decay time. The delay time here is relative to 1 January 1990, with the Mount Pinatubo eruption at 1.45 years. The final term represents the quasi-periodic solar response $\delta(z)$ in K/SFU to $Q_{81}(t)$, the 81-day averaged $F10.7$ solar flux. Note that $T_{\mathrm{fit}}(z, t)$ depends linearly on eight of the parameters but depends nonlinearly on t_0(z), t_1(z), and t_2(z). Note also, we did not include the response to quasi-biennial oscillation since its effect is apparently negligible in our data in the MLT. In performing our earlier long-term study based on the 17-year and 25-year data sets (She et al., 2009 and 2015), we did follow the procedure of Li et al. (2008) employed for long-term study of Rayleigh lidar temperatures in the stratosphere and lower mesosphere over Mauna Loa Observatory, Hawaii, and included the effect of quasi-biennial oscillation in the fit function. When applied to our long-term data set at the time, the least-squares-fit returned amplitudes much smaller than the associated statistical uncertainties. Unlike most other analysis, we include a term, $\gamma(z)P(z,t)$, for Pinatubo response observed in both our lidar (She et al., 1998) and the French lidar (Keckhut et al., 1995) after the Mount Pinatubo eruption. Therefore, the form of our fit function is constructed based on what is observed visually (thus larger than noise variations) in time series.

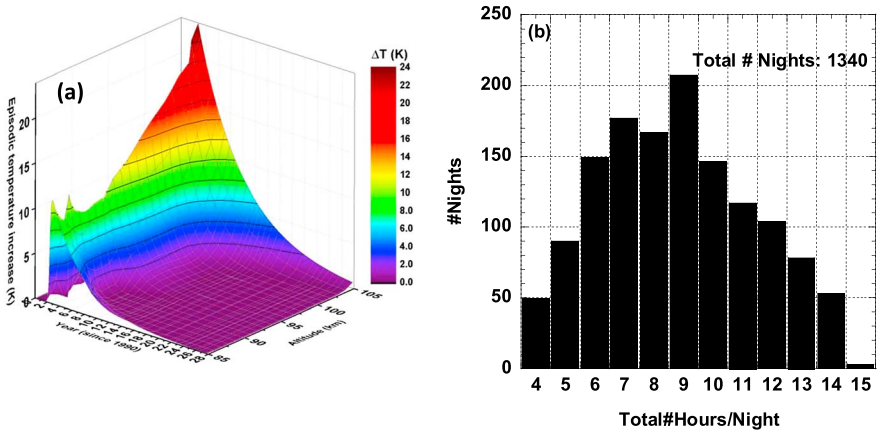

Figure 1. (a) The Pinatubo/episodic response (K) as a function of altitude (85–105 km) and time (0–28 years, since 1990) deduced from 11-parameter analysis of _Ngt(90-17). (b) The distribution of number of nights (totaling 1,340 nights) with a specified number of hours of observations.

Assessing the long-term changes or trend from a long observational data set is quite different than that from an atmospheric model, where one could assess various effects independently. For example, the linear temperature trend resulting from greenhouse gas accumulation may be assessed under perpetual solar minimum condition (Solomon et al., 2018). On the other hand, in the analysis of an observational data set both the response to solar flux variation and long-term trend must be included in the fit equation. Unfortunately, the response to solar flux is not orthogonal to the long-term trend; this leads to mutual contaminations. The only way to minimize such contamination is to have a data set long enough to cover two or more solar cycles whose temporal structures are unfortunately not the same. As we employed daily 81-day mean solar flux, we use nightly temperatures directly for the regression analysis without binning them monthly or yearly, because there exist unavoidable data gaps in the observations. Binning them otherwise may bias or shift the phase of the response under consideration. For the same reason, we include annual and semiannual variation terms. Should there be no data gap, then whether we include these terms explicitly and employ nightly, monthly, or yearly binning makes no difference.

Using the nightly mean temperatures (either _Ngt or _2MN) as the data input for the regression analysis of (1), the impact of quasi-two-day (QTD) and other planetary waves (PWs) with periods of about 5 days and 7 days in the data set was not treated and not included in $T_{fit}(z,t)$. The QTD waves known to occur in Northern Hemisphere in July and August are planetary-scale westward propagating oscillations with zonal wavenumber 3 or 4 and a period near 2 days, varying between 1.7 and 2.3 days (Salby & Callaghan, 2001). The occurrence of QTD and PWs is somewhat unpredictable, and their variable periods make the assignment of proxy base functions difficult. By using nightly means data, we clearly ignore possible contamination from diurnal tides; since the lengths of observations in about half of nights are shorter than 10 hr, see Figure 1b, we are unable to integrate out shorter-period tidal perturbations in many nights. Properly accounting for the impact of all these quasi short-period oscillations from tidal periods of 8, 12, and 24 hr to QTD and PWs is extremely difficult if not impossible. However, the manner they affect the long-term trend between the two nightly mean data sets differently may be qualitatively discussed at the end of section 3.

2.2. Two Long-Term Nocturnal Temperature Data Sets and Measurement Errors

In this paper we form two types of nightly mean data sets between 1990 and 2017. All observations throughout the night (between 4 and 15 hr depending on season and weather), are denoted as _Ngt(90-17). The 2-hr average centered at local midnight, is denoted as _2MN(90-17). The shorter data lengths were employed in our previous studies (She et al., 2009, 2015); we perform nonlinear 11-parameter least squares fits of equation (1) to _Ngt(90-17) and denote the results as F11P_Ngt(90-17). Using the four parameters $\gamma(z)$, $t_0(z)$, $t_1(z)$, and $t_2(z)$ depicting the warming episode, we construct the Pinatubo response function $\gamma(z)P(z,t)$ for all altitudes between 85 and 105 km as shown in Figure 1a. It is essential to test several initial "guesses" for the nonlinear fit parameters until the regression settles into the global least squares minimum as opposed to a local

minimum. We regard the result as satisfactory if a function $\gamma(z)P(z,t)$ has the shape of an impulse response that can be repeated with close but different initial guesses and that yields continuity as a function of z. By subtracting $\gamma(z)P(z,t)$ from the data set _Ngt(90-17), an alternative data set _Ngt-PR(90-17), where PR stands for Pinatubo response removed, is formed; its use in a seven-parameter linear regression analysis without the Pinatubo term yields results denoted as F7P_Ngt(90-17). This set of seven-parameter results are critical for our trend studies for summer and winter seasons discussed in section 3, because the data gap in either summer or winter in the 1990s is too big for a reliable extraction of the Pinatubo response, precluding an 11-parameter nonlinear regression analysis for summer or winter.

As is detailed in Krueger et al. (2015), there are two sources of measurement uncertainties. The systematic error, due mainly to the frequency locking uncertainty of lidar transmitter to an absolute frequency standard, in this case a Na Doppler-free spectrum (She & Yu, 1995) locking to an accuracy within 1–2 MHz, amounts to temperature uncertainly less than 0.2 K. The photon statistical error is a function of lidar power-aperture product, detection efficiency, and desired temporal and vertical resolution; this is altitude dependent due to the bell-shaped Na density vertical profile. Typical 1 σ uncertainty of nightly mean temperature in 2002 and before, when the PA product (with telescope diameter of 35 cm) was 0.05 Wm^2 and 20% efficient photomultipliers were used, are less than 5 K for summer nights between 85 and 97.5 km and less than 0.5 K for winter nights between 84 and 100 km. The use of 40% efficient photomultipliers and installation of two larger telescopes made the uncertainty of nightly mean temperature between 85 and 105 km rarely larger than 5K. This can be seen by examining the altitude dependence of the number of nights in the 1,340 nights of _Ngt (90-17) observations with error bars less than 5 K or 10 K (not shown), from which we can conclude, as is well known, that the Na density increases sharply from 80 to 85 km and decreases slowly above 95 km. We thus report results between 85 and 105 km.

Also of interest is the distribution of hours of observation per night for _Ngt(90-17) and _Ngt-PR(90-17) shown in Figure 1b. Depending on the season and weather conditions, the number of observational hours varied between 4 and 15. Strictly speaking, despite collecting many hours of nocturnal observations, there is tidal contamination in the _Ngt(90-17) data set, but we expect tides of 12 hr or less to be averaged out to a large extent. For this reason, we form as an alternative, the 2-hr averaged data set _2MN(90-17) centered at midnight for comparison. To facilitate better comparison of the solar response and linear trend in the two data sets, we removed the same Pinatubo contribution from the _2MN(90-17) data set, yielding _2MN-PR(90-17), and used it for the seven-parameter analysis, resulting in F7P_2MN(90-17). In summary, we perform the 11-parameter nonlinear regression fit to _Ngt(90-17) to deduce the $\gamma(z)P(z,t)$ function shown in Figure 1a, with which we deduce the Pinatubo removed full or section of time series _xx(xx-xx) from _Ngt(90-17) or _2MN(90-17). We then perform the seven-parameter linear fit to yield solar response and linear trend, denoted, respectively, as F7P_Ngt(xx-xx) or F7P_2MN(xx-xx). Depending on whether/which seasonal filter is applied to the time series in question, the resulting profile is marked by -A, -S or -W, respectively for annual, 4-month summer or 6-month winter data.

2.3. Comparison Between Original and Pinatubo-Removed Time Series and Analysis Results

The concept of two-level mesopause for the midlatitude and polar region (von Zahn et al., 1996) is characterized by minimum seasonal variation at a high altitude of ~99 km and maximum seasonal variation at a low altitude at ~86 km (She & von Zahn, 1998). Figure 2a, the temperatures time series of _Ngt(90-17) at 99 km along with the 81-day mean solar flux variation, F81_Solar Flux, shows the presence of three pieces of multiyear temporal variations. First, temperatures more-or-less follow the solar flux variation in time. Second, when averaged over solar cycles, the temperatures decrease slowly in time. And third, upon a more careful look near the first solar maximum in early 1990s, one sees a delay of temperature peak from solar flux peak by 2–3 years, suggesting an impulsive warming response after (because of) the Mount Pinatubo eruption at 1.45 years. We then plot the corresponding time series of the Pinatubo response $\gamma(z)P(z,t)$ removed data _Ngt-PR(90-17) in Figure 2b for comparison. The higher temperature points in the box bounded by 130–150 K and years 2–4 in Figure 2a are now gone (moved lower) and the temperature and solar flux time series track each other much better. Similarly, we plot 2-hr midnight means _2MN(90-17) and _2MN-PR(90-17) at 99 km in Figures 2c and 2d, respectively. The higher temperature points in the box bounded by 130–175 K and years 2–4 in Figure 2c are moved lower in Figure 2d, and again gives a better tracking to the solar flux variation.

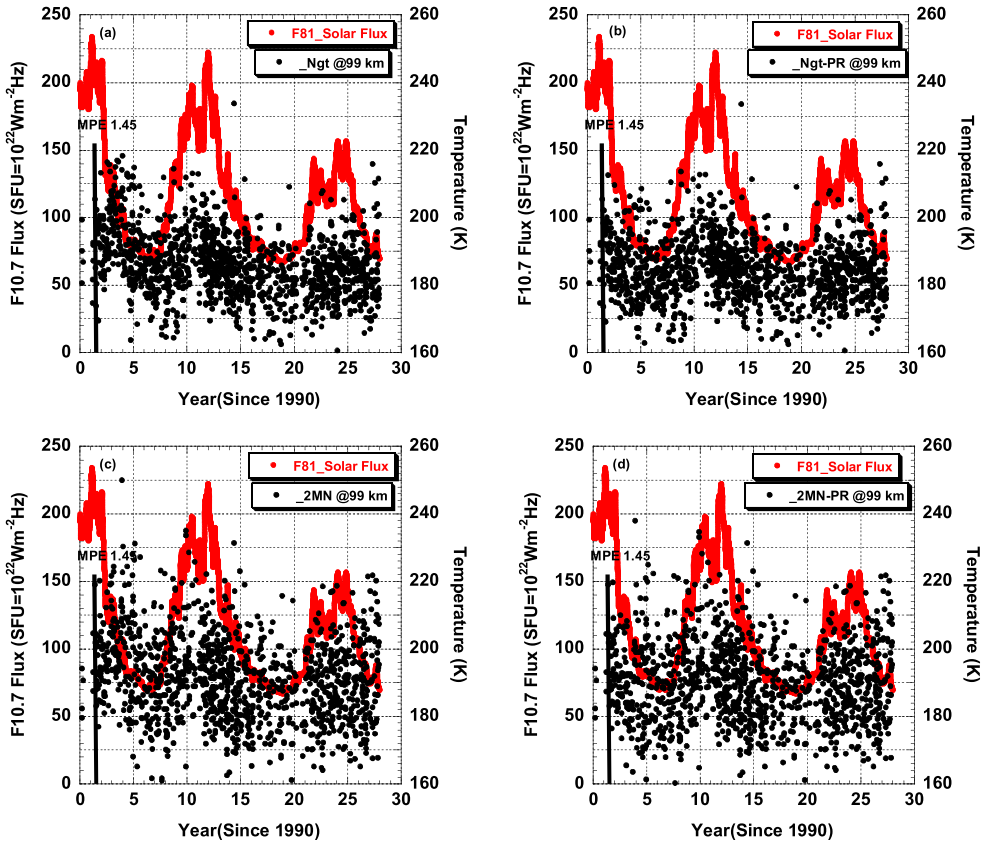

Figure 2. (a) Time series of nightly mean temperatures _Ngt at 99 km as observed plotted along solar flux from 1990 to 2017. (b) Same as (a) except with Pinatubo/episodic function, Figure 1a, removed. Panels (c) and (d) are the same as (a) and (b), respectively, except for 2-hourly mean temperatures centered at midnight _2MN.

We next consider the solar response and linear trend profiles from both 11-parameter and 7-parameter analyses of all data as profiles F11P_Ngt-A(90-17) and F7P_Ngt-A(90-17). Since the best linear regression fit of a given fit function and a data set is unique and independent of initial guesses of the fit parameters, the two best fits (not shown) are nearly identical except in the error bars. That the error bars of F7P_Ngt-A(90-17) are smaller than those of F11P_Ngt-A(90-17) is an artifact due to the exclusion of the $\gamma(z)P(z,t)$ term and associated interference in the former. To include this error contribution, the larger error bars should be used for both analyses. Therefore, for what follows, we will use the ratio of the errors (1 σ uncertainty) of F11P_Ngt-A(90-17) to that of F7P_Ngt-A(90-17) as the error correction factors (for solar response and linear trend, respectively) to prorate the error bars for all other seven-parameter fits below.

3. The Long-Term Change Deduced From Lidar Nocturnal Temperatures (1990–2017)

The best 7-parameter fit with all 28 years observational data _Ngt-PR(90-17) yields solar response and linear trend profiles denoted as F-7P_Ngt-A(90-17). Because of the well-known difference in thermal balance between winter and summer months with different solar heating (winter nights are longer) and adiabatic effect (winter warming and summer cooling) that lead to the formation of the two-level mesopause with summer shorter than winter, we are also interested in long-term changes for winter and summer months separately. Results from the seven-parameter analyses utilizing the _Ngt-PR(90-17) temperatures for the 4-month summer (May, June, July, and August, a total of 455 nights, in blue) and for the 6-month winter (October, November, December, January, February, and March, a total of 654 nights, in black) long-term analyses are shown in Figures 3a and 3b as F-7P_Ngt-S(90-17) and F-7P_Ngt-W(90-17), respectively. The error bars are prorated using the error correction factors as mentioned. Also plotted are F-7P_Ngt-A(90-17) and prorated error bars using annual data set in red for comparison. As noted, to arrive at the best fits

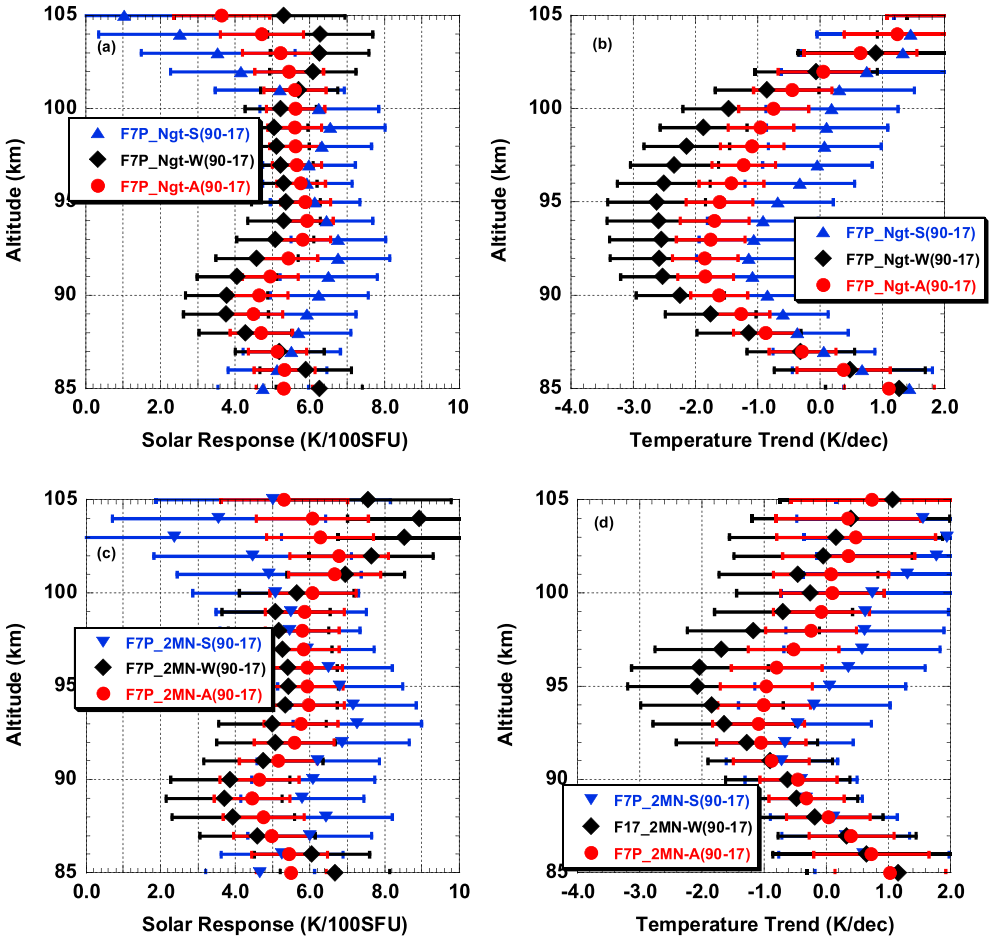

Figure 3. Solar response (a) and linear trend (b) deduced from seven-parameter regression analyses of 4-month summer (blue), 6-month winter (black), and all (red) Pinatubo/episodic function removed nightly mean temperatures _Ngt(90-17). Panels (c) and (d) are the same as (a) and (b), respectively, except for 2-hourly mean temperatures centered at midnight _2MN.

shown in Figure 3, the four terms for seasonal variations with fit parameters, $A_1(z)$,$B_1(z)$,$A_2(z)$, and $B_2(z)$ were included in (1), while they were ignored in the regression analysis of modeled data [see, e.g., Gan et al., 2017; Solomon et al., 2018]. We tested this issue by analyzing the same data sets with these terms set to zero. Since our 28-year-long lidar data sets are quite extensive, excluding the A-B terms gave differences in the resulting solar response and linear trend that were noticeable but not significant.

Even though the tidal contamination in _Ngt on long-term changes should not be large as explained in view of the distribution of hours of observation per night in Figure 1b, to reduce tidal contaminations in nighttime observations to its minimum, we use observations at a specific tidal phase and form the 2-hr averaged data set centered at midnight _2MN. This approach has been the practice when using nocturnal data of unequal length to represent daily means, as done in Clemesha et al. (2004) for example, who used mean sodium density between 1900 and 2200 local time to determine the long-term rate change of centroid height. Here, we use 2-hr means to sample the midnight tidal phase in temperature. For the same 28-year period, the _2MN data set has 453, 626, and 1,310 nights, respectively, for 4-month summer (S), 6-month winter (W), and annual (A) observations. Since the number of nights for respective groups (S, W, A) are not too different from those for nightly means, the _2MN data set could be considered as a better daily mean representative (with less tidal contamination) for long-term change study. After the removal of Pinatubo contribution, $\gamma(z)P(z,t)$, the data set _2MN-PR is used to perform seven-paramter linear regression best fits, resulting in summer, winter, and annual long-term responses, respectively, denoted as F-7P_2MN-S(90-17), F-7PR_2MN-W(90-

17), and F-7PR_2MN-A(90-17); their solar responses and linear trends with prorated error bars are shown in Figures 3c and 3d, respectively.

Comparing Figure 3c to Figure 3a, we see similar solar responses for altitudes between 85 and 100 km. Above 100 km, the solar responses from _2MN-PR data set yielded higher solar response than those deduced from _Ngt-PR data set. In particular, the 6-month winter response, F-7P_2MN-W(90-17) increases linearly from 5.6 K/100 SFU at 100 km to 8.9 K/100 SFU at 104 km as might be anticipated from a model prediction, see Figure 14 of Marsh et al. (2007), for example. Comparing Fig. 3(d) to Fig. 3(b), we see the linear trend profiles between 85 and 90 km from both data sets, _2MN-PR and _Ngt-PR are similar in shape. The altitudes at which the trend turns from cooling to warming are somewhat lower from _2MN-PR data set (at 95, 102, and 100 km) than those from _Ngt-PR data set (at 98, 102, and 102 km), respectively, for summer, winter, and annual trends. The maximum cooling for these trends is, respectively, about 0.7, 2.1, and 1.1 K/decade occurring at 91, 95, and 93 km deduced from _2MN-PR and about 1.2, 2.6, and 1.8 K/decade occurring at 92, 92, and 95 km deduced from _Ngt-PR data set. The cooling trend of F-7P_2MN-A(90-17) and F-7P_Ngt-A(90-17) are statistically significant between 91 and 96 km and between 88 and 100 km, respectively.

To appreciate the difference in the resulting trends between _Ngt and _2MN data sets, we consider the shift in the linear trend resulting from a short-period (tides, QTD or PWs) perturbation with 1-K amplitude at one altitude. If the phase of the short-period wave were constant, its contribution in the _2MN time series amounts to adding a constant to each night with data. Because the terms $\alpha(z)$, $\beta(z)t$, and $\delta(z)Q_{81}(t)$ are not orthogonal, the added constant will shift the value of $\alpha(z)$ by ~1 K with very small shifts in $\beta(z)$ on the order of 10^{-5} K/decade or less. On the other hand, the contribution of the same wave from the _Ngt time series adds various amounts to different nights with data, leading to a larger change in $\beta(z)$ on the order of 10^{-1} K/decade. Using the actual start and end observation times each night with data, we considered other scenarios of slowly varying phase and amplitude (limited to 1 K) and found the shift in trend up to 0.06 K/decade for _2MN, and 0.33K/decade for _Ngt. The differences only depend upon the time-dependent proxy base functions in (1) and the times of observation and not on the long-term fitting parameters. Given that the experimental trends are of the order of a few K/decade with uncertainties up to ±1 K/decade, this calculation supports ignoring the unknown short-period waves in $T_{\text{fit}}(z,t)$. As tides are the dominant regularly occurring global waves in the atmosphere, the difference in trends and solar responses between the two nightly data sets, _Ngt and _2MN is likely due to their difference in tidal wave sampling. In this connection, we note that the amplitudes of the SABER-observed (global) diurnal temperature tides between 80 and 95 km are less than 6 K, but they could reach 12 K at 105 km (Yuan et al., 2010). And more importantly, the seasonal variations of the both diurnal and semidiurnal total (migrating + nonmigrating) tides are dominated by the migrating tides, as shown in Figure 4 of Yuan et al. (2014). Since the phase of a migrating tide should be locked to the solar position, the phase of a diurnal or semidiurnal tide at a given altitude is nearly constant. Of course, there are day-to-day variations in nightly means, mainly resulting from (local) gravity wave interactions with tides and planetary waves (She et al., 2004); though this has not been treated in our analyses, the manner that they affect the two nightly time series should be comparable as both data sets have observations on the same nights. Therefore, the different tidal wave samplings between the two 28-year time series is likely the main cause for the max cooling shown in F-7P_2MN-A(90-17) to be about 60% of that shown in F-7P_Ngt-A(90-17), implicating it as the main factor making the trend deduced from nightly mean temperatures about twice as large as a model prediction (Laštovička, 2017).

4. The Long-Term Change Compared to SABER and LIMA Models (1979–2013)

The solar response of lidar data set at 41–42°N, F7P_Ngt-A(90-17) shown in Figure 3a in red may be compared with the extended Canadian Middle Atmosphere Model (eCMAM30) between 1979 and 2010, and with the 14-year (2002–2015) observation by SABER on board the Thermosphere Ionosphere Mesosphere and Dynamics at 40°N published in Gan et al. (2017). We compare eCMAM and SABER data between 75 and 100 km read from Figure 3 of Gan et al. (2017) to lidar data between 85 and 105 km plus the value at 81 km. We note that the eCMAM response increases from 1.5 K/100 SFU at 75 km to ~2.4 K/100 SFU at 85 km and stays there until 95 km before it almost doubled to 4.8 K/100 SFU at 100 km. On the other hand, the SABER response increases from 2.4 K/100 SFU at 75 km to a maximum of 5 K/100 SFU at 80 km then dips to a minimum of 3.4 K/100 SFU at 85 km; it then increases again to 4.4 K/100 SFU at 90 and 95 km

before it decreases to ~ 2 K/100 SFU at 100 km. As expected, the eCMAM response increases considerably as it reaches altitudes of 100 km and above, but both lidar and SABER responses decrease, respectively, at 105 and 100 km. Most interesting and ironic is that both vertical profiles of lidar and SABER undergo a similar up and down pattern with lidar about 5 km higher. We offer no explanation for this apparent coincidence. The F-7P_2MN-A(90-17) solar response as shown in Figure 3c is similar to that of the F-7P_Ngt-A(90-17) in Figure 3a except that the response decreases less at the ends of the vertical profile, that is, 105 km, where the number of nights with data are less and thus are more likely to be susceptible to tidal contamination. We suspect the tidal contamination is even more difficult to assess for SABER as it needs 60 days of observation to complete 24 hr of global local time observation. In addition, we note that the vertical profile of solar response for summer, F-7P_Ngt-S(90-17) in Figure 3a, peaks between 90 and 100 km and decreases considerably at both ends at 81 km (3.07 ± 1.66 K/100 SFU, not shown) and 105 km (1.03 ± 2.45 K/100 SFU). Connecting this bell-shaped solar response in the MLT with earlier midlatitude observations by incoherent scatter radar above and Rayleigh lidar below the altitudes reported here, one could see clear observational evidence of dynamical influences throughout different layers of Earth's atmosphere (Chanin et al., 1989; She & Krueger, 2004). This behavior seems to hold for F7P_2MN-S(90-17) in Figure 3c as well. The winter responses above 100 km in F7P_2MN-W(90-17), as seen in Figure 3c is however considerably different from those in F7P_Ngt-W(90-17) in Figure 3a. Here, between 100 and 104 km, the former increases linearly while the latter remains nearly the same as altitude increases, suggesting that above 100 km, the lidar winter solar response without tidal contamination like the models, as seen in the eCMAM (Gan et al., 2017) and Figure 14b of Marsh et al. (2007), also increases monotonically with altitude.

The lidar linear trend (1990–2017) from all data, either F7P_Ngt-A(90-17) or F-7P_2MN-A(90-17) may be compared to the SABER trend (2002–2012) at 40°N read from the lower-left panel of Figure 2 in Huang et al. (2014), roughly as starting from negligible value at ~75 km to a maximum cooling of ~2.3 K/decade at ~90 km and turning to a warming trend above ~95 km. The lidar summer trend (S) can be compared to the LIMA model for summer months at 40°N (1961–2009) read from the left panel of Figure 11 in Lübken et al. (2013), roughly as starting from a negligible warming trend at 85 km, which decreases to zero and becomes a cooling trend at ~90 km and maximizes to 0.8 K/decade at ~93 km, then becomes positive again at ~97 km. Although the detailed vertical dependences from lidar and SABER and LIMA are different, there exists a clear similarity in the shape of the vertical profile. Considering the fact that the nocturnal temperature trend (based on either _Ngt or _2MN) is comparable to SABER and LIMA trends which cover different periods and included daytime temperatures, these trends are consistent with one another.

The LIMA is a model of the middle atmosphere, which especially aims to represent the thermal structure around mesopause altitudes (*Berger*, 2008). It is a fully nonlinear, global, and three-dimensional Eulerian grid point model, which is driven by European Centre for Medium-Range Weather Forecasts reanalysis below ~40 km and extends from the ground to the lower thermosphere (0–150 km). The model considers major processes of radiation, chemistry, and transport with parameterizations of radiative transfer, including CO_2 increase and O_3 change. Due to their continued interest in the long-term evolution of noctilucent clouds (Lübken et al., 2018), the model has been concentrated on summer months and had applied to the study of summer temperature trends in the mesosphere for the period of 1961 to 2009 (Berger & Lübken, 2011; Lübken et al., 2013), resolving the impact of ozone changes. The LIMA model has recently been extended from 2009 to 2013. To reduce the statistical errors for this study, we calculate the LIMA zonal-mean temperature trends for the 4-month summer (MJJA) at 40.5°N between 1979 and 2013. The summer LIMA trend, starting from a cooling trend of 0.70 K/decade to a maximum of 0.87 K/decade at 91 km and turning positive at 100 km is compared to the corresponding local nightly mean (_Ngt) and 2-hr midnight mean (_2MN) lidar temperature trends at 41–42°N, 105–112°W between 1990 and 2017. The resulting comparisons are shown in Figure 4 as open-circles, solid triangles, and solid inverted triangles, respectively, for LIMA-S(97-13), lidar-Ngt-S(90-17), and lidar-2MN-S(90-17). Compared to LIMA, lidar summer nightly mean trends between 90 and 102 km are nearly identical; though within the LIMA error bars, they are more positive outside this range. The trend of the lidar 2-hr midnight means, though within LIMA's error bars between 88 and 100 km, are comparable to the nightly mean trend below 88 km and follow the nightly mean trend above 100 km, but more positive by ~1 K/decade. We note the maximum cooling trends of LIMA, lidar-Ngt and lidar-2MN are in excellent agreement, occurring at (91, 92, and 91) km with trends (−0.87 ± 0.76, − 1.14 ± 0.85, and − 0.71 ± 0.89) K/decade, respectively. Considering the lidar vertical

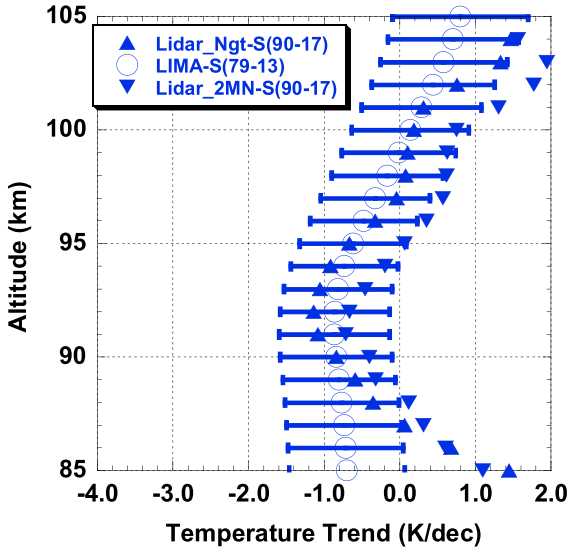

Figure 4. Comparison between LIMA (1979–2013) and lidar (1990–2017) trends of the 4-month (MJJA) summer. The LIMA summer trend in blue open circle (error bars in blue) is compared to summer lidar trends of nightly mean (_Ngt) and 2-hr midnight mean (_2MN) temperatures in blue solid triangles (for error bars, see Figure 3b) and in blue solid inverted triangles (for error bars see Figure 3d), respectively.

resolution of 2 km and the different periods covered, (1979–2013) for LIMA and (1990–2017) for lidar, these trend profiles are basically in agreement, well within one another's error bars (for lidar summer trend error bars, see Figures 3b and 3d) except below 87 km. The discrepancy in trends at 85–87 km is puzzling as the lidar measurement uncertainties at these altitudes are still quite small.

5. Discussion

In addition to possible tidal and short-period wave contaminations, there are contaminations in linear temperature trend due to the interference with solar flux variation and Pinatubo warming resulting from the not-long-enough data set used for the analysis. In this section, using lidar observations, we will discuss these possible contaminations. These will be followed by a qualitative account on the influence of gravity wave dynamics on the difference between lidar summer and winter trend observations, as well as a comparison between lidar data sets from 1990 versus from 1996 to 2017 to assess the impact of stratospheric ozone change on the linear temperature trend at the MLT.

5.1. Length of Data Set for Reliable Trend Analysis

In a recent review, Laštovička (2017) noted "that 11 years is a relatively short period for establishing reliable trends due to presence of various other influences of predominantly atmospheric/meteorological origin." Since the solar flux term and the linear trend term in the fit function (1) are not orthogonal and the solar flux function $Q_{81}(t)$ is different from one solar cycle to the next, we use our 28-year-long data set to show the need to use data set longer than two solar cycles for a reliable trend analysis. For this purpose, we can use either _Ngt-PR (xx-xx) or _2MN-PR (xx-xx) data sets, but we opted for the former in part to better relate to our previous publications.

Shown in Figure 5a are linear trends from three data sets about 10–11 years long, (96-08) from solar min to solar min of Cycle 23 in blue, (02-14) from solar max of Cycle 23 to solar max of Cycle 24 in black triangles, and (02-12). The same 10-year duration in black inverted triangles were used, for example, by Hall et al. (2012), when they studied trend at 90 km over Svalbard, Norway (78°N, 16°E). These are compared to the trend deduced from the full lidar data set (90-17) in red. It is clear the trends from shorter data sets show cooler trend with max cooling at different altitudes by as much as 2.5 K/decade. On the other hand, the linear trends from the three data sets covering about two solar cycles long, as shown in Figure 5b, (90-14) in blue, (94-17) from solar min of Cycle 23 to solar min of Cycle 24 in black triangles, and (91-15) from solar

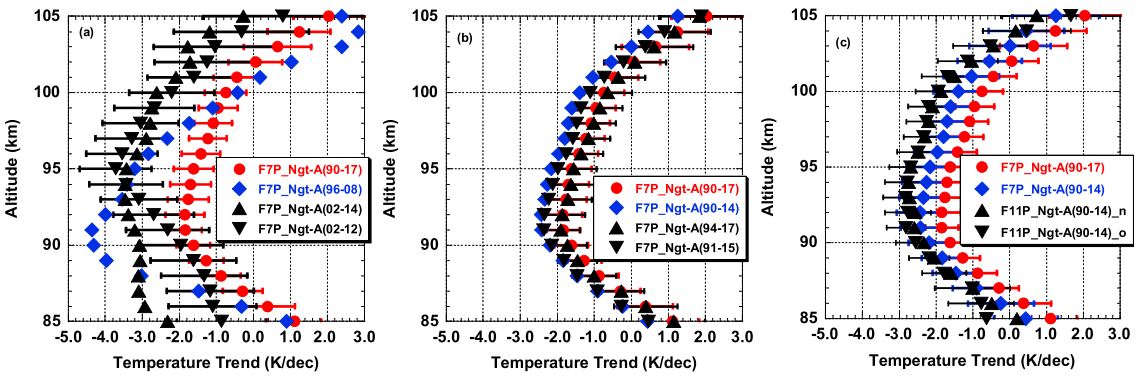

Figure 5. Comparison of linear trends of nightly mean nocturnal temperatures in different duration cuts from the same data set Ngt-PR(90-17), (a) and (b), and with different Pinatubo functions in (c). (a) Three trends with data about one solar cycle long compared to that of full length. (b) Three trends with data about two solar cycles long compared to that of full length. (c). Three linear trends between 1990 and 2014 deduced from data with different Pinatubo response functions compared to the trend of full-length data (90-17). See text for more details.

max of Cycle 22 to solar max of Cycle 24 in black inverted triangles, though not identical, are basically the same as the trend deduced from the full data set (90-17) in red with a maximum difference of about 0.5 K/decade. We point out that all data sets used in Figure 5 are different duration cuts from _Ngt-PR(90-17) with the Pinatubo response function shown in Figure 1a removed from the observed data set _Ngt(90-17).

5.2. Effect of Pinatubo/Episodic Response Functions

To investigate the subtle difference between the deduced Pinatubo response functions, we first note in Figure 5b the difference in maximum cooling trends deduced from the 25-year data set F7P_Ngt-A (90-14) in blue and the 28-year data set F7P_Ngt-A(90-17) in red with rates of -2.44 ± 0.63 K/decade at 92 km and of -1.89 ± 0.51 K/decade at 91 km, respectively. This difference is the result of data length and associated solar flux variability, as both data sets, _Ngt-PR(90-14) and _Ngt-PR(90-17) were derived from the same original data set __Ngt(90-17) by removing the same Pinatubo response function, as shown in Figure 1a. Since the data set before Pinatubo removal _Ngt(90-14) is the same as the data set used for the published trend (She et al., 2015), one might expect the resulting trend between F7P_Ngt-A(90-14) and that shown as F11P(90-14)_Avg in Figure 2 of She et al. (2015) to be the same. However, they are not quite the same as shown in Figure 5c between F7P_Ngt-A(90-14) in blue repeated, and F11P(90-14)_Avg as F11P_Ngt-A(90-14)_o in black inverted triangles; the maximum trend for the former is -2.44 ± 0.63 K/decade at 92 km, while that for the latter is -2.80 ± 0.58 K/decade at 91–93 km (She et al., 2015). In fact, the entire former trend profile shows less cooling than that of the latter, by more than 0.5 K/decade between 95 and 100 km. The interference between Pinatubo response function and the linear trend is to blame for this discrepancy. The Pinatubo response function of the former, was deduced from F11P_Ngt-A(90-17) analysis using the full data set of 28 years, while that of the latter was deduced from F11P_Ngt-A(90-14)_o analysis using the 25-year data set __Ngt(90-14) with the old Pinatubo response function given in Figure 3a of She et al. (2015). Both the length of the data sets and "best" initial guesses for the nonlinear parameters for the two 11-parameter nonlinear analyzes are different! If we repeat the F11P_Ngt-A(90-14) analysis with the same "best" initial guess as that used for F11P_Ngt-A(90-17) analysis, we obtained a new Pinatubo function and the associated linear trend for the 25-year data set shown as F11P_Ngt-A(90-14)_n in Fig. 5(c) in triangles. Notice that the different "best" initial guesses (same data set) as we compared black triangles and black inverted triangles in Fig. 5(c) yields linear trends that are not identical, but are basically the same (except near the ends of the profile) with max trends at 91-93 km, respectively, of -2.80 ± 0.58 and -2.60 ± 0.59 K/decade. That using the different data lengths with the same initial guess for the nonlinear regression fit leads to different results does not imply that the Pinatubo response lasted beyond some 20 years. It simply reflects the fact that with noise in the data, the interference of the Pinatubo response could lead to an uncertainty in trend of ~0.5 K/decade. The linear trend using all data (90-17) for both trend and Pinatubo response determination yields the trend profile in red circles, which as shown in Figure 5c is about 1 K/decade less cooling than the three trends with shorter duration (90-14). We point out that the two Pinatubo functions in the _Ngt(90-14) are essentially the same as that shown in Figure 1a, with only minor differences at the altitude edges.

5.3. Gravity Wave Activities and the Lidar Differential Summer and Winter Trends

As shown in Figures 3b and 3d, the linear trend is more negative in winter months than in summer months. That the maximum cooling trend for the 6-month winter is more than twice as large as that for the 4-month summer may be appreciated by noting that in the MLT, the winter mean temperatures are warmer and that the wave perturbations are more pronounced than those in summer months, see, for example, Lübken and von Zahn (1991), Keckhut et al. (1995), and in Figures 4c and 5 of Gardner and Liu (2007). Higher winter mean temperatures yields more cooling for the same percentage of cooling. The impact of dynamical effects on seasonal difference in temperature trend is not as straightforward and requires further investigation. In particular, larger cooling trend in winter appears to be contrary to the well-known gravity wave influence on mean-state temperatures with larger effects in summer, causing the formation of cool summer mesopause. As is by now well known that the upward propagation, growth, and breaking of gravity waves (GWs) of varied frequency and wavelength deposits momentum and heat in the atmosphere, impacting upper atmospheric dynamics greatly, causing adiabatic and diabatic (turbulence) circulation and heating, affecting global mean-state climatology. Since our knowledge of the source and dynamics of these gravity waves is incomplete, the effects of GW activities on climatology are modeled, for example, by schemes of gravity

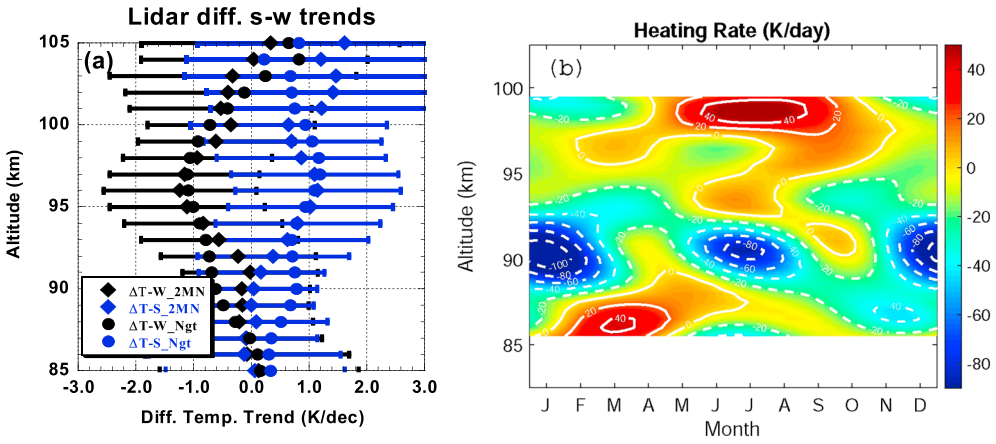

Figure 6. (a) Profiles of Lidar differential summer (blue) and winter (black) trends, solid diamonds for _2MN and solid circles for _Ngt. Notice strictly speaking, the altitudes for statistically summer/winter difference lie between 93 and 99 km. (b) Heating rate resulting from heat flux convergence of gravity wave activities observed from New Mexico (35°N, 106.5°W) taken from Figure 13, Gardner and Liu (2007).

wave parameterization as in WACCM (Garcia et al., 2017). In this case, a tuning or nudging process is typically applied to yield model outputs in agreement with reanalyzed lower atmospheric observations. Consequently, their deposition of momentum in the background MLT, leading to adiabatic flows from summer pole to winter pole, has correctly predicted cold summer and warm winter mesopause, but the impact of gravity wave (GW) with such a treatment on diverse aspects of atmospheric dynamics remains an important source of uncertainty. Relevant to this paper on local long-term temperature trend, however, is the effect of GW heat flux and turbulence generated by GW breaking, as well as their associated long-term trends. Unfortunately, the observation of these quantities is very challenging, and are rare to non-existence. We know GW heat flux divergence leads to adiabatic local heating/cooling at different vertical heights, and the associated turbulence generated by GW breaking leads to diabatic local heating with associated energy propagation yielding adiabatic heating/cooling elsewhere. Lübken (1997) determined the turbulent energy dissipation rate for summer and winter months at high latitudes by measuring in situ neutral density fluctuations, Gardner and Liu (2007) measured GW heat flux by lidar at midlatitude from which seasonal distribution of MLT heat flux divergence (or heating/cooling rate) was determined, and more recently, based on limited lidar observations, Guo et al. (2017) suggested that the heat transport from one region to another caused by GW heat flux convergence (adiabatic) is larger than turbulence heat dissipation (diabatic) and associate heat flux transport (adiabatic). Here, we term turbulence heating as real heating but call adiabatic heating/cooling due to heat flux divergence (by GWs or turbulence) as dynamical effects. Regardless of the magnitude of turbulence heating, without the knowledge of the long-term trend of turbulence, its contribution to long-term temperature trend cannot be assessed. Fortunately, there is a paper on the trend of GW variance at midlatitude in both summer and winter (Jacobi, 2014), so we can shed some light on the contribution of GW dynamical effects on long-term temperature trend below.

To facilitate the evaluation of GW dynamical effects on lidar-observed long-term trend and associated summer-winter difference, we note that the long-term temperature trend is primarily the result of the change in greenhouse gas content in the atmosphere. To simplify the problem, we assume the dynamical effects of GWs are the main cause for the summer/winter trend difference. Since GW activity is weak near equinox (April and September), the summer/winter trend difference may be investigated by comparing the differences in summer and winter trends (relative to the annual temperature trend) as plotted in Figure 6a, the profiles of lidar differential summer (blue) and winter (black) trends, solid diamonds for _2MN, and solid circles for _Ngt. Since the differences between these two lidar data sets is minimal, and for simplicity, we discuss the summer and winter trend differential profiles, with the _2MN(90-17) data set, (ΔT-S_2MN) and (ΔT-W_2MN). To qualitatively account for these summer/winter trend differences, we invoke the rare observations of the seasonal distribution in heat flux heating rate at the nearby Starfire Optical Range, NM (35°N, 106.5°W) by Gardner and Liu (2007), and on the trend of GW variance based

on 24-year (1984–2007) Collm (52°N, 13°E) wind measurements (Jacobi, 2014). As the altitude range of available heat flux heating rate in Figure 13 of Gardner and Liu (2007), of the trend on GW variance in Figure 5a of Jacobi (2014) and observed differential trends in Figure 6a are all different, we can only point out the connections between these observation and Figure 6a and hope to reveal effects of GW heat flux divergence on the observed summer/winter trend difference.

Inspection of Figure 6a suggests that the difference between (ΔT-S_2MN) and (ΔT-W_2MN) may be divided into three altitude ranges, between 85 and 90 km, between 91 and 99, and between 100 and 105 km. The differences in trend behaviors are nearly zero between 85 and 90 km, positive for summer, and negative for winter with nearly equal magnitude between 91 and 99 km, which gradually increases from zero at 91 km to a maximum of ~1 K/decade and decreases to ~0.5 K/decade at 99 km. For the altitude range of 100 to 105 km, both differential trends gradually become more positive as altitude increases, with winter from –0.4 K/decade to +0.8 K/decade, and summer from 0.6 K/decade to 1.6 K/decade. As pointed out in Gardner and Liu (2007), the strong downward heat transport in both summer and winter leads to "strong cooling centered around 90 km" with a larger cooling rate in winter than in summer. The observed GW heat flux heating rate distribution with clear winter/summer differences is more clearly shown in Figure 13 of Gardner and Liu (2007), repeated here as Figure 6b. Though in different altitude ranges, we can also divide Figure 6b into three sections, 85–87 km with negligible heating/cooling rate in 6-month winter (note cancelation between January-February-March and October-November-December) and in 4-month summer, 88–93 km with large cooling rate (winter stronger than summer) and 94–100 km with strong heating rate in summer and weak cooling rate in winter. The seasonal dependence in GW variance trends between 85 and 93 km as observed in Collm shown in Figure 5a of Jacobi (2014) is negative for the 4-month summer and positive for 6-month winter. Coupling the heat flux heating/cooling rate with the GW variance trend between 88 and 93 km, the dynamical effect could indeed lead to cooling (warming) in winter (summer) differential trends, or much stronger cooling trend in winter than in summer, consistent with the behavior of the 91–99 km section of Figure 6a. The heat flux heating/cooling rate is negligible in both summer and winter, consistent with the behavior of the 85–90 km region (at least for the _2MN profiles) of Figure 6a. While we do not find observational data for GW variance trend above 95 km, the heating rate observation suggests the existence of a scenario that could be consistent with the statistically insignificant difference observation between 100 and 105 km as shown in Figure 6a with summer warming more than winter by as much as 2 K/decade. Since the extent of the dynamical effect included in the summer/winter difference in the observed trends is not exactly known, our discussion here intends to point out what might affect the difference rather than to account for it.

A caveat for using the trend on GW variance elsewhere for this work is in order. After investigating the published works on the trends of atmospheric waves, Laštovička (2017) concluded that these trends are "substantially regionally dependent" and they are "not stable with time". Without anything better, we use the observation at Collm as proxy as it is the result of 24 years of observation with overlapping altitudes which allows deduction of both 4-month summer and 6-month winter long-term GW variance trends. In Figure 5 of a more recent publication on GW variance trends based on 14 years (2002–2015) of SABER temperatures (Liu et al., 2017), the altitude-height of linear GW trend is displayed between 50°S and 50°N for each month. Although the conclusion "The significant positive trend of GWs at around 50°N during July is consistent with that derived from medium-frequency radar observations in the height range of 80–88 km" {presumably referred to Hoffmann et al. (2011), who reported the trend of GW variance (period 3–6 hr) between 1990 and 2010 at Juliusruh (55°N, 13°E) in July at this height range to be positive} does not agree with the observed negative July trend in Jacobi (2014), their signs for the 4-month summer and 6-month winter GW trends are consistent. Figure 5 of Liu et al. (2017) between 85 and 95 km of 40–50°N shows larger negative trends in May and June than the positive trends in July and August, giving rise to a net negative 4-month summer GW trend; similarly, it shows positive trends in November, December, and March with nearly zero trends in October, January, and February, giving rise to a net positive 6-month winter trend. Another potential problem is that, unlike the lidar measurements, which has resolutions as fine as 2 min and 1 km (Gardner & Liu, 2007), the trend analysis of GW variances reported so far were unable to include GW activities with periods shorter than ~2 hr. Though lidar observations at several sites including ours are now long enough for the desired trend analysis, unfortunately, they have not yet appeared in the literature and thus are begging for future study.

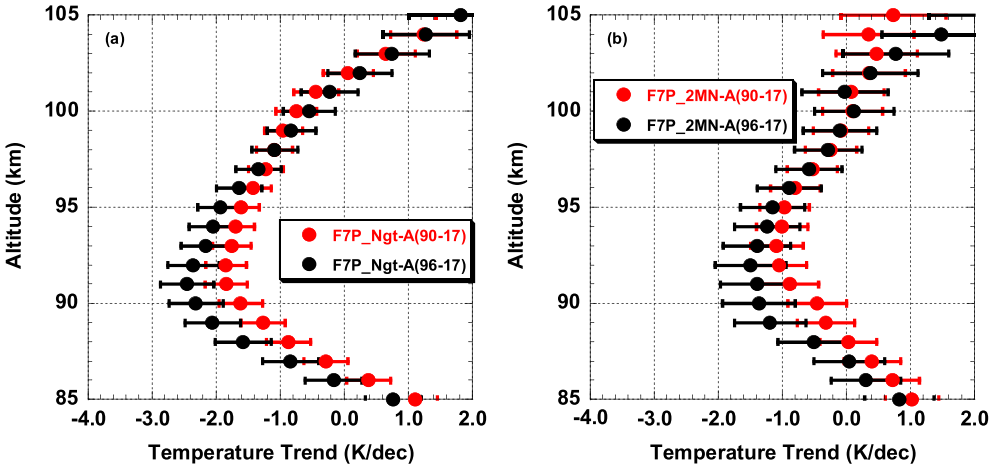

Figure 7. Linear temperature trend comparison between periods (1990–2017) in red and (1996–2017) in black; the former includes 6 years at the end of the dramatic stratospheric ozone depletion, while the latter is entirely after ozone recovery; (a) based on nightly means _Ngt and (b) based on 2-hr midnight means _2MN.

5.4. Impact to Stratospheric Ozone Change in Midlatitude Temperature Trend

The existence of the Antarctic stratospheric ozone hole between 1979 and 1995, and its partial recovery since the end of 1995 is well known. analyzing the total ozone record of five European stations near 50°N, Krzyscin et al. (2005) also find similar trend changes. Among other things, changes in the low-frequency ionospheric reflection height have been observed to accompany this dramatic ozone concentration variation (Bremer & Peters, 2008). These ozone changes have also been incorporated into the radiation budget of global change modeling as for example in LIMA [Berger and Lübken et al., 2011; Lübken et al., 2013]. Unfortunately, our 28-year-long lidar observation contains only 6 years (1990–1995) of data in this period (1979–1995), not long enough to assess the long-term temperature trends before and after the end of 1995 separately. One way to acknowledge the presence of different trends in different periods is to replace the linear trend term by either a bilinear term (Berger & Lübken, 2011) with a break point or by a linear plus a quadric term (Keckhut et al., 2011), and perform eight-parameter regression analysis with the entire data set. This can certainly be done mathematically. However, in either case, the two terms in the replacement fit function are not orthogonal, and inevitably lead to very large error bars. Instead, we perform seven-parameter trend analyzes on Pinatubo removed nightly mean and 2-hr midnight mean data sets for periods (1990–2017) and (1996–2017), that is,_Ngt-PR(90-17), _Ngt-PR(96-17), _2MN-PR(90-17), and_2MN-PR(96-17), and compare the trend results between two _Ngt data sets in Figure 7a and two _2MN data sets in Figure 7b. In either case, the profiles of red circles, F7P_Ngt-A(90-17) and F7P_2MN-A(90-17) are repeats of those in Figures 3b and 3d, respectively. The corresponding profiles of black circles, F7P_Ngt-A(96-17) and F7P_2MN-A(96-17) are the linear trends after ozone recovery. It is clear in both cases, while the black and red circles are within each other's error-bars at both ends of the profiles, the black points are more negative than the red points between 87and 93 km for _Ngt trends and between 88 and 91 km for _2MN trends, with a difference as much as ~1 K/decade, reflecting the partial effect of ozone recovery at these altitude range. The same analysis on solar responses (not shown) for (90-17) and (96-17) yielded the solar cycle effect within each other's error-bars.

Since cumulative cooling causes shrinking, a constant pressure level comes down to lower altitudes in the middle and upper atmosphere. Thus, it would be of interest if the long-term trend of a constant pressure level can be observed, exhibiting atmospheric shrinking directly. Like the low-frequency ionospheric reflection height, the mesopause is thought to form at a constant pressure level in winter mainly due to radiative cooling, and the other in summer, controlled mostly by the adiabatic cooling. Indeed, very recently, the long-term trends on the altitude and temperature of the high (winter, HM) and low (summer, LM) mesopause, based on the same Na lidar observations without removal of Pinatubo function and with the addition of data in 2018 has been published (Yuan et al., 2019). As shown in Figure 1a, the Pinatubo response near the mesopauses after 2000 is much reduced. They compared data sets between (1990–2018) and (2000–2018) and

found the dropping of HM height at the speed of about 450 m/decade for both data sets, while the LM trend is statistically insignificant. Meanwhile, the mesopause temperature shows a cooling trend of more than ~2 K/decade for both HM and LM since 1990, but it has become considerably less and statistically insignificant after 2000.

6. Conclusions

We have presented regression analyses of solar response and the linear trend based on a Na lidar nocturnal temperature observations at midlatitude between 1990 and 2017 in two groups, nightly mean temperatures, _Ngt, and 2-hr midnight mean temperatures, _2MN, to shed light on the potential tidal bias. The solar response _Ngt and _2MN, are comparable, around 5 ± 1 K/100 SFU with higher summer response, similar to our previous results for shorter data durations. The _2MN trends start from positive values at about 88 km, go through a negative minimum and then go back positive around 100 km. Compared to the _2MN trends, the trend deduced from _Ngt temperatures are cooler generally by ~1 K/decade. The observed solar response and linear trend between 1990 and 2017 and those from SABER temperatures between 2002–2014 and 2002–2012 are in general agreement. The linear lidar summer trends (1990–2017), lidar-Ngt and lidar-2MN, are within the error-bars of LIMA 1979–2013 trend predictions. Between 89 and 100 km, the LIMA trend is nearly identical to the lidar-Ngt trend. We note the maximum cooling trends are within one another's error bars. Invoking the gravity wave heat flux convergence observations at a nearby lidar station and the trend observations of midlatitude GW variance, this study reveals a likely link between GW dynamical effects and the summer/winter difference in the observed lidar temperature trends.

Using our 28-year-long data set, we investigate the interference by other atmospheric variations and conclude that a data set longer than two solar cycles is necessary for a reliable deduction of linear (long-term) trend. We also revealed that along with the migrating tidal dominance in our lidar site, the potential tidal (and short-period waves) contamination may double the max cooling rate (from 1 K/decade to 2 K/decade), and that the various determinations of the Pinatubo/episodic function from a long data set may lead to 0.5 K/decade discrepancy in linear trend. Though our data set only covered about 6 years (1990–1995) at the end of the dramatic ozone depletion period (1979–1995), it reveals a more negative linear trend since 1996 as the result of stratospheric ozone recovery by as much as 1 K/decade at 90 km.

Acknowledgments

This study was supported in part by the Strategic Priority Research Program of Chinese Academy of Sciences (Grant XDA17010303). The work in Germany is supported by the German BMBF project TIMA as a part of the ROMIC program. The CSU/USU Na lidar project is supported by National Science Foundation grants AGS-1041571, AGS-1135882, AGS-1734333 and AGS-1136082. The lidar data used in this study, CSU (1990–2010) and USU (2010–2017) are available from the CEDAR madrigal database (http://cedar.openmadrigal.org/list/). The lead author acknowledges many helpful and generous discussions with Rashid Akmaev and Rolando Garcia on long-term change in the MLT. He also thank Alan Liu and Hanli Liu for discussions on the associated dynamical forcing, and the former for providing an improved copy of Figure 6b. F. J. L. and U. B. acknowledge fruitful discussions with Gerd Baumgarten.

References

Akmaev, R. A., & Fomichev, V. I. (1998). Coupling of the mesosphere and lower thermosphers due to doubling of CO_2. *Annales Geophysicae*, *16*, 1501–1512.

Akmaev, R. A., Fomichev, V. I., & Zhu, X. (2006). Impact of middle atmospheric composition changes on greenhouse cooling in the upper atmosphere. *Journal of Atmospheric and Solar-Terrestrial Physics*, *68*(17), 1879–1889. https://doi.org/10.1016/j.jastp.2006.03.008

Beig, G. (2006). Trends in the mesopause region temperature and our present understanding—An update. *Physics and Chemistry of the Earth*, *31*, 3–9.

Beig, G. (2011). Long-term trends in the temperature of the mesosphere/lower thermosphere region: 1. Anthropogenic influences. *Journal of Geophysical Research*, *116*, A00H11. https://doi.org/10.1029/2011JA016646

Berger, U. (2008). Modeling of middle atmosphere dynamics with LIMA. *Journal of Atmospheric and Solar-Terrestrial Physics*, *70*(8-9), 1170–1200. https://doi.org/10.1016/j.jastp.2008.02.004

Berger, U., & Lübken, F.-J. (2011). Mesospheric temperature trends at mid-latitudes in summer. *Geophysical Research Letters*, *38*, L22804. https://doi.org/10.1029/2011GL049528

Bremer, J., & Peters, D. (2008). Influence of stratospheric ozone changes on long-term trends in the meso- and lower thermosphere. *Journal of Atmospheric and Solar-Terrestrial Physics*, *70*(11–12), 1473–1481. https://doi.org/10.1016/j.jastp.2008.03.024

Chanin, M.-L., Keckhut, P., Hauchecorne, A., & Labitzke, K. (1989). The solar activity Q.B.O. effect in the lower thermosphere. *Annals of Geophysics*, *7*, 463–470.

Clemesha, B. R., Simonich, D. M., Batista, P. P., Vondrak, T., & Plane, J. M. C. (2004). Negligible long-term temperature trend in the upper atmosphere at 23_S. *Journal of Geophysical Research*, *109*, D05302. https://doi.org/10.1029/2003JD004243

Cnossen, I. (2012). Climate change in the upper atmosphere, Chap. 15. Greenhouse gases – emission, measurement and mangement, edited by Liu, G. http://www.intechopen.com/books/greenhouse-gases-emission-measurement-and-management/climate-change-in-the-upper-atmosphere

Gan, Q., Du, J., Fomichev, V. I., Ward, W. E., Beagley, S. R., Zhang, S., & Yue, J. (2017). Temperature responses to the 11 year solar cycle in the mesosphere from the 31 year (1979–2010) extended Canadian Middle Atmosphere Model simulations and a comparison with the 14 year (2002–2015) TIMED/SABER observations. *Journal of Geophysical Research: Space Physics*, *122*, 4801–4818. https://doi.org/10.1002/2016JA023564

Garcia, R. R., Marsh, D. R., Kinnson, D. E., Boville, B. A., & Sassi, F. (2007). Simulation of secular trends in the middle atmosphere, 1950–2003. *Journal of Geophysical Research*, *112*, D09301. https://doi.org/10.1029/2006JD007485

Garcia, R. R., Smith, A. K., Kinnison, D. E., Cámara, Á. D. L., & Murphy, D. J. (2017). Modification of the gravity wave parameterization in the Whole Atmosphere Community Climate Model: Motivation and results. *Journal of the Atmospheric Sciences*, *74*(1), 275–291. https://doi.org/10.1175/JAS-D-16-0104.1

Gardner, C. S., & Liu, A. Z. (2007). Seasonal variations of the vertical fluxes of heat and horizontal momentum in the mesopause region at Starfire Optical Range, New Mexico. *Journal of Geophysical Research*, *112*, D09113. https://doi.org/10.1029/2005JD006179

Guo, Y., Liu, A. Z., & Gardner, C. S. (2017). First Na lidar measurements of turbulence heat flux, thermal diffusivity, and energy dissipation rate in the mesopause region. *Geophysical Research Letters*, *44*, 5782–5790. https://doi.org/10.1002/2017GL073807

Hall, C. M., Dyrland, M. E., Tsutsumi, M., & Mulligan, F. J. (2012). Temperature trends at 90 km over Svalbard, Norway (78°N 16°E), seen in one decade of meteor radar observations. *Journal of Geophysical Research*, *117*, D08104. https://doi.org/10.1029/2011JD017028

Hoffmann, P., Rapp, M., Singer, W., & Keuer, D. (2011). Trends in mesospheric gravity waves at northern middle latitudes during summer. *Journal of Geophysical Research*, *116*, D00P08. https://doi.org/10.1029/2011JD015717

Holmen, S. E., Hall, C. M., & Tsutsumi, M. (2016). Neutral atmosphere temperature trends and variability at 90 km, 70°N, 19°E, 2003–2014. *Atmospheric Chemistry and Physics*, *16*(12), 7853–7866. https://doi.org/10.5194/acp-16-7853-2016

Huang, F. T., Mayr, H. G., Russell, J. M. III, & Mlynczak, M. G. (2014). Ozone and temperature decadal trends in the stratosphere, mesosphere and lower thermosphere, based on measurements from SABER on TIMED. *Annals of Geophysics*, *32*(8), 935–949. https://doi.org/10.5194/angeo-32-935-2014

Jacobi, C. (2014). Long-term trends and decadal variability of upper mesosphere/lower thermosphere gravity waves at midlatitudes. *Journal of Atmospheric and Solar-Terrestrial Physics*, *118*, 90–95. https://doi.org/10.1016/j.jastp.2013.05.009

Kalicinsky, C., Knieling, P., Koppmann, R., Offermann, D., Steinbrecht, W., & Wintel, J. (2016). Long-term dynamics of OH* temperatures over central Europe: Trends and solar correlations. *Atmospheric Chemistry and Physics*, *16*(23), 15033–15047. https://doi.org/10.5194/acp-16-15033-2016

Keckhut, P., Hauchecorne, A., & Chanin, M. L. (1995). Midlatitude longterm variability of the middle atmosphere: Trends and cyclic and episodic changes. *Journal of Geophysical Research*, *100*(D9), 18,887–18,897. https://doi.org/10.1029/95JD01387

Keckhut, P., Randel, W. J., Claud, C., Leblanc, T., Steinbrecht, W., Funatsu, B. M., et al. (2011). An evaluation of uncertainties in monitoring middle atmosphere temperatures with the ground-based lidar network in support of space observations. *Journal of Atmospheric and Solar-Terrestrial Physics*, *73*(5-6), 627–642. https://doi.org/10.1016/j.jastp.2011.01.003

Krueger, D. A., She, C.-Y., & Yuan, T. (2015). Retrieving mesopause temperature and line-of-sight wind from full-diurnal-cycle Na lidar observations. *Applied Optics*, *54*(32), 9469–9489. https://doi.org/10.1364/AO.54.009469

Krzyscin, J. W., Jaruslawski, J., & Rajewska-Wiech, B. (2005). Beginning of the ozone recovery over Europe? Analysis of the total ozone data from the ground-based observations, 1964–2004. *Annales Geophysicae*, *23*(5), 1685–1695. https://doi.org/10.5194/angeo-23-1685-2005

Laštovička, J. (2013). Trends in the upper atmosphere and ionosphere: recent progress. *Journal of Geophysical Research: Space Physics*, *118*, 3924–3935. https://doi.org/10.1002/jgra.50341

Laštovička, J. (2017). A review of recent progress in trends in the upper atmosphere. *Journal of Atmospheric and Solar-Terrestrial Physics*, *163*, 2–13. https://doi.org/10.1016/j.jastp.2017.03.009

Li, T., Leblanc, T., & McDermid, I. S. (2008). Interannual variations of middle atmospheric temperature as measured by the JPL lidar at Mauna Loa Observatory, Hawaii (19.5_N, 155.6_W). *Journal of Geophysical Research*, *113*, D14109. https://doi.org/10.1029/2007JD009764

Liu, X., Yue, J., Xu, J., Garcia, R. R., Russell, J. M. III, Mlynczak, M., et al. (2017). Variations of global gravity waves derived from 14 years of SABER temperature observations. *Journal of Geophysical Research: Atmospheres*, *122*, 6231–6249. https://doi.org/10.1002/2017JD026604

Lübken, F.-J. (1997). Seasonal variation of turbulent energy dissipation rates at high latitudes as determined by in situ measurements of neutral density fluctuations. *Journal of Geophysical Research*, *102*(D12), 13,441–13,456. https://doi.org/10.1029/97JD00853

Lübken, F.-J., Berger, U., & Baumgarten, G. (2013). Temperature trends in the midlatitude summer mesosphere. *Journal of Geophysical Research: Space Physics*, *118*, 13,347–13,360. https://doi.org/10.1002/2013JD020576

Lübken, F.-J., Berger, U., & Baumgarten, G. (2018). On the anthropogenic impact on long-term evolution of noctilucent clouds. *Geophysical Research Letters*, *45*, Paper 19 (1 – 9(13), 6681–6689. https://doi.org/10.1029/2018GL077719

Lübken, F. J., & von Zahn, U. (1991). Thermal structure of the mesopause region at polarlatitudes. *Journal of Geophysical Research*, *96*, 20,841–20,857.

Marsh, D. R., Garcia, R. R., Kinnison, D. E., Boville, B. A., Sassi, F., Solomon, S. C., & Matthes, K. (2007). Modeling the whole atmosphere response to solar cycle changes in radiative and geomagnetic forcing. *Journal of Geophysical Research*, *112*, D23306. https://doi.org/10.1029/2006JD008306

Offermann, D., Hoffmann, P., Knieling, P., Koppmann, R., Oberheide, J., & Steinbrecht, W. (2010). Long-term trends and solar cycle variations of mesospheric temperature and dynamics. *Journal of Geophysical Research*, *115*, D18127. https://doi.org/10.1029/2009JD013363

Qian, L., Marsh, D., Merkel, A., Solomon, S. C., & Roble, R. G. (2013). Effect of trends of middle atmosphere gases on the mesosphere and thermosphere. *Journal of Geophysical Research: Space Physics*, *118*, 3846–3855. https://doi.org/10.1002/jgra.50354

Roble, R. G., & Dickinson, R. E. (1989). How will changes in carbon dioxide and methane modify the mean structure of the mesosphere and lower thermosphere? *Geophysical Research Letters*, *16*(12), 1441–1444. https://doi.org/10.1029/GL016i012p01441

Salby, M., & Callaghan, P. (2001). Seasonal amplification of the 2-day wave: relationship between normal mode and instability. *Journal of the Atmospheric Sciences*, *58*(14), 1858–1869. https://doi.org/10.1175/1520-0469(2001)058<1858:SAOTDW>2.0.CO;2

She, C. Y., & Krueger, D. A. (2004). Impact of natural variability in the 11-year mesopause region temperature observation over Fort Collins, CO (41N, 105W). *Advanced Space Physics*, *34*(2), 330–336. https://doi.org/10.1016/j.asr.2003.02.047

She, C.-Y., Krueger, D. A., Akmaev, R., Schmidt, H., Talaat, E., & Yee, S. (2009). Long-term variability in mesopause region temperatures over Fort Collins, CO (41_ N, 105_ W) based on lidar observations from 1990 through 2007. *Journal of Atmospheric and Solar-Terrestrial Physics*, *71*(14-15), 1558–1564. https://doi.org/10.1016/j.jastp.2009.05.007

She, C.-Y., Krueger, D. A., & Yuan, T. (2015). Long-term midlatitude mesopause region temperature trend deduced from quarter century (1990–2014) Na lidar observations. *AnGeo Communications*, *33*, 363–369. https://doi.org/10.5194/angeocom-33-363

She, C. Y., Li, T., Collins, R. C., Yuan, T., Williams, B. P., Kawahara, T. D., et al. (2004). Tidal perturbations and variability in the mesopause region over Fort Collins, CO (41N, 105W): Continuous multi-day temperature and wind lidar observations. *Geophysical Research Letters*, *31*, L24111. https://doi.org/10.1029/2004GL021165

She, C. Y., Thiel, S. W., & Krueger, D. A. (1998). Observed episodic warming at 86 and 100 km between 1990 and 1997: Effects of Mount Pinatubo eruption. *Geophysical Research Letters*, *25*(4), 497–500. https://doi.org/10.1029/98GL00178

She, C. Y., & von Zahn, U. (1998). The concept of two-level mesopause: Support through new lidar observation. *Journal of Geophysical Research*, *103*(D5), 5855–5863. https://doi.org/10.1029/97JD03450

She, C. Y., & Yu, J. R. (1995). Doppler-free saturation fluorescence spectroscopy of Na atoms for atmospheric applications. *Applied Optics*, *34*(6), 1063–1075. https://doi.org/10.1364/AO.34.001063

Solomon, S. C., Liu, H.-L., Marsh, D. R., McInerney, J. M., Qian, L., & Vitt, F. M. (2018). Whole atmosphere simulation of anthropogenic climate change. *Geophysical Research Letters*, *45*, 1567–1576. https://doi.org/10.1002/2017GL076950

Yuan, T., She, C.-Y., Krueger, D. A., Reising, S., Zhang, X., & Forbes, J. M. (2010). A collaborative study on temperature diurnal tide in the midlatitude mesopause region (41°N, 105°W) with Na lidar and TIMED/SABER observations. *Journal of Atmospheric and Solar-Terrestrial Physics*, *72*(5-6), 541–549. https://doi.org/10.1016/j.jastp.2010.02.007

Yuan, T., She, C. Y., Oberheide, J., & Krueger, D. A. (2014). Vertical tidal wind climatology from full-diurnal-cycle temperature and Na density lidar observations at Ft. Collins, CO (41 ° N, 105° W). *Journal of Geophysical Research: Atmospheres*, *119*, 4600–4615. https://doi.org/10.1002/2013JD020338

Yuan, T., Solomon, S. C., She, C.-Y., & Krueger, D. A. (2019). The long-term trends of nocturnal mesopause temperature and altitude revealed by Na lidar observations between 1990 and 2018 at mid-latitude. *Journal of Geophysical Research: Atmospheres*, *124*. https://doi.org/10.1029/2018JD029828

von Zahn, U., Hoffner, J., Eska, V., & Alpers, M. (1996). The mesopause altitude: Only two distinct levels worldwide? *Geophysical Research Letters*, *23*(22), 3231–3234. https://doi.org/10.1029/96GL03041